

Spectrum-tailorable two-dimensional silicon–titanium nitride selective emitter by photon recycling for thermophotovoltaic applications

Xiaoqi Zhou¹, Man Zhang¹, Shengyu Sun, Yixin Sun¹, Zhongyan Li¹, Shipei Zhang, Xiawa Wang^{*}

Division of Natural and Applied Sciences, Duke Kunshan University, Kunshan, Jiangsu, 215316, China

ARTICLE INFO

Keywords:

Nanosphere lithography
Photonic crystal
Selective emitter
High-temperature application
Thermophotovoltaic system

ABSTRACT

Thermophotovoltaic (TPV) systems have gained attention for their ability to convert radiant energy from heat sources into electricity. One major challenge is fabricating a spectrum-tailorable selective emitter with high performance at elevated temperatures. In this study, two-dimensional (2D) silicon-titanium nitride (Si-TiN) photonic crystals (PhCs) with TiN-coated Si cavities were fabricated using nanosphere lithography (NSL). The lossy nature and high reflectivity of TiN in the long-wavelength range allow the Si-TiN PhC to achieve up to ~92% broadband optical emissivity (200 nm – cut-off wavelength) while minimizing heat radiation to ~27% in the long-wavelength range (5 – 10 μm). More importantly, thanks to the isotropy of the NSL method based on oxygen plasma etching (OPE), different periods and radius of the Si-TiN PhC can be achieved by controlling the OPE time or the initial polystyrene sphere diameter. This enables precise control over the cut-off wavelength and emission spectrum to match various PV cells. The 2D Si-TiN PhC produced 3.13 times more power than a flat Si emitter. This approach provides a promising path forward for enhancing TPV system performance and practical applications.

1. Introduction

Thermophotovoltaic (TPV) systems that use high-temperature heat sources to produce electricity are promising for future batteries with widespread commercial applications [1–4], which typically consisting of a heat source, a radiator, a filter, and thermophotovoltaic cells. Within a TPV system, the heat released from the source, which can be from radioisotope, combustion or solar concentrator, emits infrared radiation to be collected and converted by a low-bandgap solar cell [5–7]. Spectral control using selective emitters has been a well-known technology to increase the efficiency of thermal-to-electricity conversion [8–10]. With the advancements in nano-photonics and micro-nano fabrication technologies over recent decades, selective emitters have transitioned from bulk and rare-earth metal-doped emitters, to one-dimensional (1D) multilayer films [11–15], to higher-dimensional photonic crystal metamaterials [16–21]. Among these, 1D multilayer emitters can be fabricated with large areas. However, the thermal stability of these emitters was constrained by the mismatch of thermal expansion coefficients between the layers [22]. In contrast, 3D emitters have garnered significant attention due to their high spectral selectivity [23]. Nonetheless, the intricate geometries and complex fabrication processes result in high manufacturing costs [24].

Compared to other types of emitters, 2D PhCs fabricated on refractory metals have shown excellent optical performance, thermal stability and fabrication feasibility [10,25]. Typically made from tungsten or tantalum, these crystals leverage the metals' high reflectivity in the long-wavelength range [17,26]. Periodic micro-fabricated cavities were patterned so that electromagnetic waves with the resonant modes can be coupled to increase emissivity, thus enhancing emission for in-band energy conversion [27,28]. By tailoring the cavities' radius, periodicity, and depth, 2D PhCs can be optimized for thermophotovoltaic cells with different bandgaps [29,30].

However, two main challenges limit the broader use of 2D PhCs: the lithography methods and the substrate materials. To fabricate the periodic structures suitable for TPV applications, past research mostly used nanoimprint and interference lithography (IL) followed by deep reactive ion etching [31,32]. Nanoimprint lithography needs E-beam writing of the pattern on a template, which not only increases the cost for larger areas but also limits the flexibility to adjust the pattern parameters. Interference lithography employs two coherent light sources to produce fringes that define the pattern. This method requires a finely tuned recipe, which cannot be easily transferred to different facilities.

* Corresponding author.

E-mail address: xiawa.wang@dukekunshan.edu.cn (X. Wang).

¹ X. Zhou and M. Zhang contributed equally to this work.

Additionally, the process of deep etching refractory metals requires specialized facilities and techniques, which are often inaccessible in standard laboratories, hindering their widespread development. Compared to refractory metals, the patterning and deep etching of silicon (Si) is much easier to allow different structures, including cavities, pillars, cones, etc [33]. However, due to the bandgap limitations of bulk Si, these structures need to be further passivated with a high reflective layer to recycle photons in the deep holes while suppressing the emission in the out-of-band infrared region [34].

Therefore, in this study, nanosphere lithography (NSL) was employed to pattern Si-based 2D PhC emitters. The NSL technique offers significant flexibility in tuning the hole radius and periodicity of the pattern while also facilitating the fabrication of larger areas. Furthermore, titanium nitride (TiN) was utilized to enhance the emission of Si cavities while suppressing photons in the long-wavelength region. The emitter fabricated using the NSL method has comparable performance with the conventional nanoimprint method, showing little impact by the defects intrinsic to this method. Finally, the successful application of Si-TiN PhC in a TPV system demonstrated a substantial increase in output power, achieving a value 3.13 times greater than that of a flat Si emitter.

2. Experimental section

2.1. Si-TiN PhC fabrication

The fabrication procedure of the Si-TiN PhC involved polystyrene (PS) sphere self-assembly, oxygen plasma etching (OPE), electron beam evaporation, deep reactive ion etching (DRIE) and magnetron sputtering. PS spheres were self-assembled into hexagonally close-packed arrays on the Si substrates via floating-transferring method [35]. The diameters of the PS spheres were reduced by plasma cleaner (PC-300, SAMCO) at 150 W with a 20 sccm O₂. Subsequently, a 328 nm thick silicon dioxide (SiO₂) hard etch mask was deposited by electron beam evaporation at a deposition rate of 1 Å/s (ei-5z, ULVAC Co., Ltd.). The PS spheres were removed through sonication in toluene, ethanol, and deionized water. The mask pattern was subsequently transferred into the Si substrates via DRIE (RIE-400iPB, SAMCO) using a modified Bosch process, details of which have been described in previous studies [36–38]. After pattern transfer, the residual SiO₂ mask was removed by inductively coupled plasma (ICP) etching (HAASRODE-E200A, Leuven Inc.) under a CHF₃ (20 sccm)/Ar (30 sccm) atmosphere with an ICP/Bias power of 300 W/100 W and a chamber pressure of 8 mTorr. Finally, a TiN film was deposited onto the Si cylindrical cavities by reactive radio frequency magnetron sputtering (CS-200z, ULVAC Co., Ltd.), performed at 0.1 Pa at 600 W with Ar and N₂ flow rates of 56 and 14 sccm, respectively. The substrate was heated to 300 °C and rotated to ensure uniform film deposition.

For the fabrication of nanoimprinted Si-TiN PhC samples, the imprinting process was performed by Suzhou Guangduo Micro Nano Devices Co., Ltd, whereas the other steps were the same as those employed for the NSL-based Si-TiN PhC.

2.2. TPV experiment

A custom-designed TPV system consisting of an electric heat source, an emitter, a photovoltaic (PV) cell, and a cooling plate was utilized to evaluate the practical applicability of the Si-TiN PhC. The electric heater consists of a 0.5 mm diameter tantalum wire encased in a molybdenum shell heated by a DC power supply (UTP16020, LINI-T). A triple-junction GaInP₂/InGaAs/Ge PV cell by Shanghai Full suns Co., Ltd was used to convert photons into electricity. The gap between the emitter and the PV cell was maintained at 1.4 cm. The output power was obtained from the maximum power point of the I-V sweep taken using a precision source-meter (2636B, Keithley Instruments Inc.). To minimize conductive and convective heat losses, the entire system was maintained in a vacuum at pressures below 0.1 Pa.

2.3. Characterization

The top-view and side-view scanning electron microscopy (SEM) images of our samples were acquired using field emission scanning electron microscopy (Gemini 500, Zeiss). The optical properties of our fabricated samples in the ranges of 200 – 2500 nm and 1282 – 11 000 nm were measured at room temperature using an ultraviolet-visible-near-infrared (UV-Vis-NIR) spectrometer with a 60 mm integrating sphere spectrophotometer (UV-3600 Plus + UV-2700, Shimadzu) and a Fourier-transform infrared spectrometer (FTIR, Nicolet iS50, ThermoFisher) with an integrating sphere, respectively. The external quantum efficiency (EQE) data of the solar cell were measured using the solar-cell spectral response measurement system (QE-R, EN-LITECH).

3. Results and discussion

The fabrication process of Si-TiN PhC is illustrated in Fig. 1a. To fabricate the PhC using the NSL method, Si substrates were coated with a monolayer of close-packed PS spheres with an initial diameter of 1.68 μm through the floating-transferring method (Fig. 1b). The hexagonally arranged PS monolayer was then etched using oxygen plasma to reduce the PS sphere diameter to the desired mask size. Subsequently, a SiO₂ hard mask was fabricated by depositing SiO₂ and removing the PS spheres (Fig. 1c). Then, the mask pattern was transferred into the Si substrates by DRIE and the residual SiO₂ mask was removed by ICP. The smooth sidewalls of the cavity are seen in the cross-sectional view in Fig. 1d due to the highly anisotropic nature of DRIE. Finally, Si-TiN PhC with cylindrical cavity arrays was obtained after magnetron sputtering (Fig. 1e and f), with a period $a = 1.68 \mu\text{m}$, radius $2r = 1.13 \mu\text{m}$, and cavity depth $d = 4.3 \mu\text{m}$. More experimental details are described in the experimental section. The distribution of TiN in the cavity was analyzed using scanning electron microscopy-energy dispersive spectrometry (SEM-EDS) mapping. As illustrated in Fig. 1g, most of the TiN was deposited on the top of the cavity, attributed to the high aspect ratio of the holes [39].

Fig. 2a shows that the EDS line analysis determined the TiN film's deposition depth to be approximately 2 μm. The TiN signal at the bottom of the cavity, whereas the EDS line scan results for the Si cavity, presented in Figure S1a, revealed no TiN signal. Therefore, it can be inferred that a small amount of TiN was deposited at the bottom of the cavity. Figure S1b presents a high-magnification SEM image verifying approximately 10 nm of TiN film at the bottom of the cavity. Finally, the structure of Si-TiN PhC is depicted in Fig. 2b, with TiN films coated on both the top and bottom surfaces of the Si cavity.

To characterize the optical performance of the fabricated Si-TiN PhC, its transmission and reflection spectrum was measured at room temperature from 200 nm to 2500 nm using a UV-Vis-NIR spectrometer. According to Kirchhoff's law, the emissivity/absorptivity equals one minus the reflectivity and transmissivity. Therefore, reducing reflectivity and transmissivity can enhance emission. As shown in Figures 2b and c, due to the high reflectivity of TiN [40], incident photons can be reflected and recycled, resulting in the transmittance of the Si-TiN PhC being reduced to zero compared to the Si PhC. Furthermore, due to the cavity resonance effect, the Si PhC with cylindrical cavity exhibits low reflectivity up to 1000 nm, as shown in Fig. 2c [27]. However, the low reflectivity range of the pure Si PhC is constrained by its energy gap (1.12 eV) [41]. This is also verified by the simulated electric field distribution of the pure Si cavity shown in Fig. 2e. At 800 nm, the electric field inside the cavity is strong, whereas at 2000 nm, the cavity exhibits poor coupling. Consequently, when the wavelength exceeds 1000 nm, the Si-TiN PhC still exhibits strong emission, as illustrated in Fig. 2c. Fig. 2d shows the good agreement between measured (black line) and simulated (black dashed line) emission spectra of the Si-TiN PhC emitter. The simulated electric field distribution within the TiN-coated Si cavity is strong at both visible

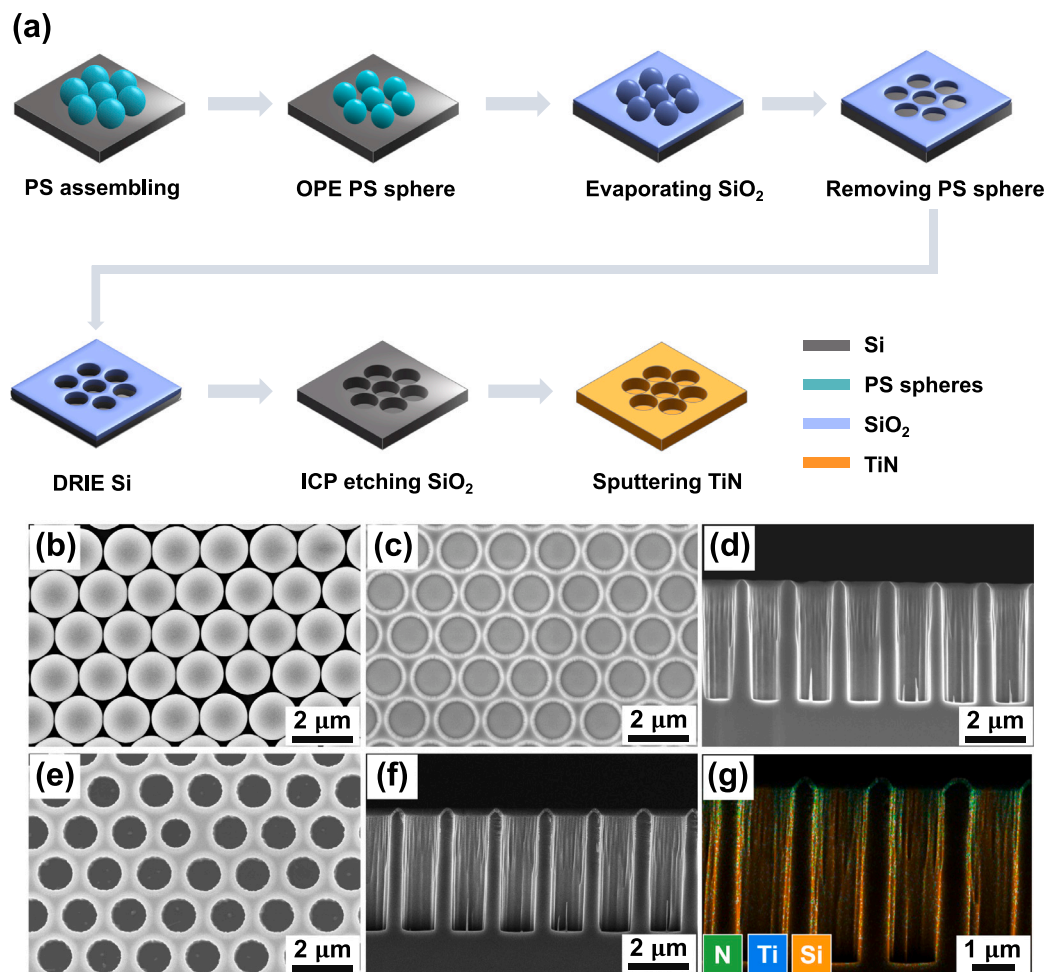


Fig. 1. (a) Schematic outline of the fabrication process for Si-TiN PhC. (b) SEM image of hexagonally packed PS sphere monolayer. (c) SEM image of SiO₂ mask. (d) Cross-sectional SEM image of Si PhC. (e) SEM image of Si-TiN PhC. (f) Cross-sectional SEM image of Si-TiN PhC. (g) EDS mapping image of N, Ti, and Si, respectively.

to near-infrared range due to TiN's lossy property, surface plasmonic resonance and photon recycling for cavity coupling [42], shown in Fig. 2f. Moreover, TiN is a transition-metal compound, exhibiting the properties of refractory ceramic, including a high melting temperature, chemical stability, and mechanical durability [40,43]. This makes it particularly suitable as a selective emitter for the high-temperature environment of TPV applications.

To improve optical performance, the Si-TiN PhC was optimized with varying depth. For 2D PhC with cavities, the depth of the holes typically determines the interaction between the incoming photon and the materials. Therefore, a deeper hole is almost always better for higher emission, which makes a Si-based PhC more advantageous because it is much easier to etch than others. As illustrated in Figure S2a-c, Si-TiN PhCs with depths of 1.3, 4.3, and 6.7 μm were fabricated by adjusting the number of DRIE cycles. In the cavity with a depth of 1.3 μm , some incompletely etched Si dendrites were observed. With an increase in etching cycles, the Si dendrites were further etched away and cavity depth increased. However, the thickness of the cavity walls gradually decreased, rendering them less suitable for high-temperature environments. Figure S3a illustrates that the emissivity of Si-TiN PhCs increases with cavity depth. Over the average emissivity range of 200 – 2500 nm, the Si-TiN PhC with a depth of 4.3 μm exhibits a 4.7% higher emissivity compared to that of 1.3 μm , while the Si-TiN PhC with a depth of 6.7 μm showed only a 2.4% increase over the 4.3 μm depth, as detailed in Table S1. Considering the structural stability

at high temperatures, a Si-TiN PhC depth of 4.3 μm was chosen as the optimal depth. As a selective emitter, it is crucial not only to enhance emissivity within the bandgap of the PV cells but also to suppress thermal radiation out of the bandgap. Therefore, as illustrated in Figure S2d-f, TiN films of varying thicknesses were constructed with a high degree of uniformity and density. The emissivity in the infrared region of TiN films of various thicknesses was measured using an FTIR spectrometer, as shown in Figure S3b. The average emissivity values are presented in Table S1, the 200 nm TiN film shows a 12.1% decrease compared to the 90 nm TiN film, while the 272 nm film shows only a 1.7% decrease compared to the 200 nm TiN film. Therefore, a deposition thickness of 200 nm was chosen as optimal.

As NSL is a maskless lithography process, the cavity periods and radius can be adjusted based on the sphere diameter choice and OPE time to match different PV cells. As shown in Fig. 3a, the uniformity and isotropy of the NSL method based on OPE can well control the pattern parameters [44]. This allows for precise design of the period (a) and radius (r) of the photonic crystal, corresponding to different cut-off wavelengths and thereby matching PV cells with various bandgaps, such as InGaAsSb (bandgap = 0.547 eV or $\lambda_{\text{bg}} = 2.250 \mu\text{m}$), GaSb (bandgap = 0.72 eV or $\lambda_{\text{bg}} = 1.708 \mu\text{m}$) [45], and InGaAs (bandgap = 0.45 – 0.75 eV or $\lambda_{\text{bg}} = 1.65 – 2.76 \mu\text{m}$) [46]. Fig. 3b-d depict Si-TiN PhCs with diameters of 1.33 μm (Si-TiN PhC sample I), 1.15 μm (Si-TiN PhC sample II), and 1.13 μm (Si-TiN PhC sample III) respectively, achieved by varying the OPE time to 3, 5, and 6 min.

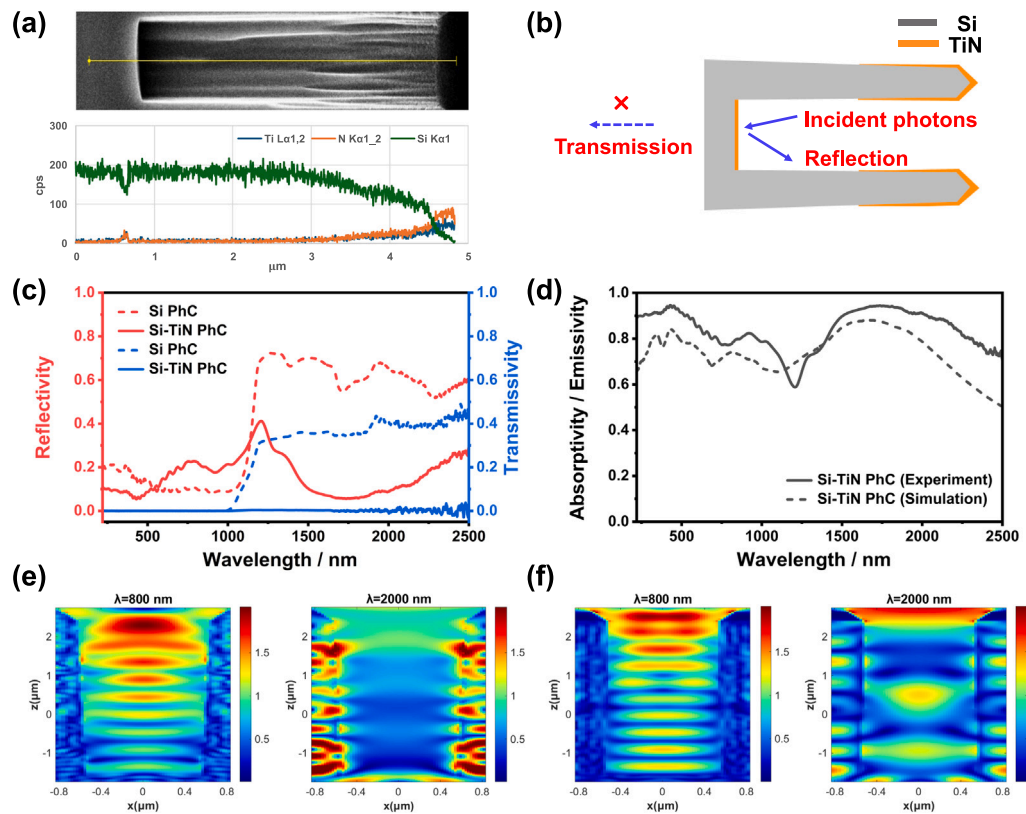


Fig. 2. (a) Cross-sectional SEM image of Si-TiN PhC with line scan for SEM-EDS. (b) Schematic representation of Si-TiN PhC structure. (c) Measured reflectivity spectra of Si and Si-TiN PhC. (d) Emission spectra of measured (black line) and simulated (black dashed line) Si-TiN PhC. (e–f) Simulated electric field distribution of the Si and Si-TiN PhC at 800 nm and 2000 nm.

These Si-TiN PhCs employed the same initial PS sphere, resulting in the same periodicity of $a = 1.68 \mu\text{m}$. Fig. 3e illustrates a Si-TiN PhC with a diameter of $0.73 \mu\text{m}$ (Si-TiN PhC sample IV), obtained by adjusting the initial PS sphere diameter to $1.17 \mu\text{m}$ and setting the OPE time to 4 min. As shown in Fig. 3f–g, Si-TiN PhCs with different diameters exhibit different cut-off wavelengths. As shown in Table 1, the relationship between cut-off wavelength and radius follows $r \approx 1.8412 \times \frac{\lambda_c}{2\pi}$ [47]. Due to differences in the settings and measurement mechanism of the UV and FTIR equipment, the spectrum is interrupted at $1.8 \mu\text{m}$ and $2.5 \mu\text{m}$, the extrapolated middle regime is shown with dotted lines as shown in Fig. 3f–g [48]. Furthermore, Fig. 3f shows that as the radius of the Si-TiN PhC increases, higher porosity facilitates greater photon emission, thereby enhancing in-band emission. However, the decrease in TiN surface coverage reduces out-of-band reflectivity, which in turn increases out-of-band emission. As detailed in Table 1, when the porosity decreases from 58.57% to 44.05%, in-band emissivity decreases by 4.56%, and emissivity in the $5 - 10 \mu\text{m}$ decreases by 9.36%. When the porosity further decreases to 40.99%, in-band emissivity decreases by only 2.74%, and emissivity in the $5 - 10 \mu\text{m}$ drops by 3.84%. To achieve larger shifts in the cut-off wavelength, smaller initial PS sphere can be used. As illustrated in Fig. 3g, when the PS sphere diameter is reduced from $1.68 \mu\text{m}$ to $1.17 \mu\text{m}$, the cut-off wavelength decreases from $2.0 \mu\text{m}$ (Si-TiN PhC sample III) to $1.5 \mu\text{m}$ (Si-TiN PhC sample IV) with similar levels of in-band high emission and out-of-band low reflection.

Compared to other methods such as photolithography, electron beam lithography, focused ion beam lithography, and nanoimprinting, the NSL-based periodic nanostructures offer advantages of low cost, high throughput, and ease of control without the need of complex equipment [49]. However, due to the inherent diameter variations of the PS spheres and non-tight packing in the self-assembly process, nanostructures patterned using the NSL method are more susceptible to defects. To investigate the impact of defects on the optical performance

of Si-TiN PhCs, the device fabricated using this method was compared with the same structure fabricated using nanoimprinting, as shown in Figure S4. As depicted in Fig. 4a, the nanoimprinted Si-TiN PhC has the same diameter of $0.73 \mu\text{m}$ as the NSL-based Si-TiN PhC and exhibits a similar porosity. Therefore, we compared the emissivity within the cut-off wavelength of 1500 nm for both structures. As shown in Fig. 4b, the emissivity of the NSL-based Si-TiN PhC (87.4%) and the nanoimprinted Si-TiN PhC (86.8%) are nearly identical. Thus, the defects in the NSL-based Si-TiN PhC have minimal impact on its optical performance.

To evaluate the practical application potential of our Si-TiN PhC, the device was put inside a TPV system and compared with a flat Si emitter as illustrated in Fig. 5a. The Si-TiN PhC and flat Si used as emitters in the TPV system were both sized at $2 \text{ cm} \times 2 \text{ cm}$. The TPV testing device consists of a vacuum chamber specifically engineered to minimize heat transfer through convection and to prevent the high-temperature oxidation of the emitter. Water coolers serve as a heat sink to cool the backsides of the PV cell. The ability to achieve radiation temperatures as high as 1373 K with notably low input power is by careful sizing of the emitter and areas covered by multilayer insulators, as shown in Fig. 5a [50]. A tantalum heating filament encased in a molybdenum shell served as the heat source, with Si-TiN PhC sample II placed on top of the heater as the emitter. The Si-TiN PhC was heated by controlling the input power of the power supply, and the photocurrent generated by the $1 \text{ cm} \times 1 \text{ cm}$ GaInP₂/InGaAs/Ge triple-junction PV cell was recorded. To ensure a good view factor, the PV cell was maintained at 1.4 cm above the emitter, and the TPV setup was maintained in a vacuum environment to minimize conductive and convective heat losses [51]. For the triple-junction GaInP₂/InGaAs/Ge cell used in our experiment, we characterized its EQE as shown in Figure S5. Fig. 5b compares the radiation spectrum of a blackbody, a flat Si, and a Si-TiN PhC at 1373 K . The radiation spectrum of the flat Si and Si-TiN PhC was derived by multiplying the 1373 K blackbody

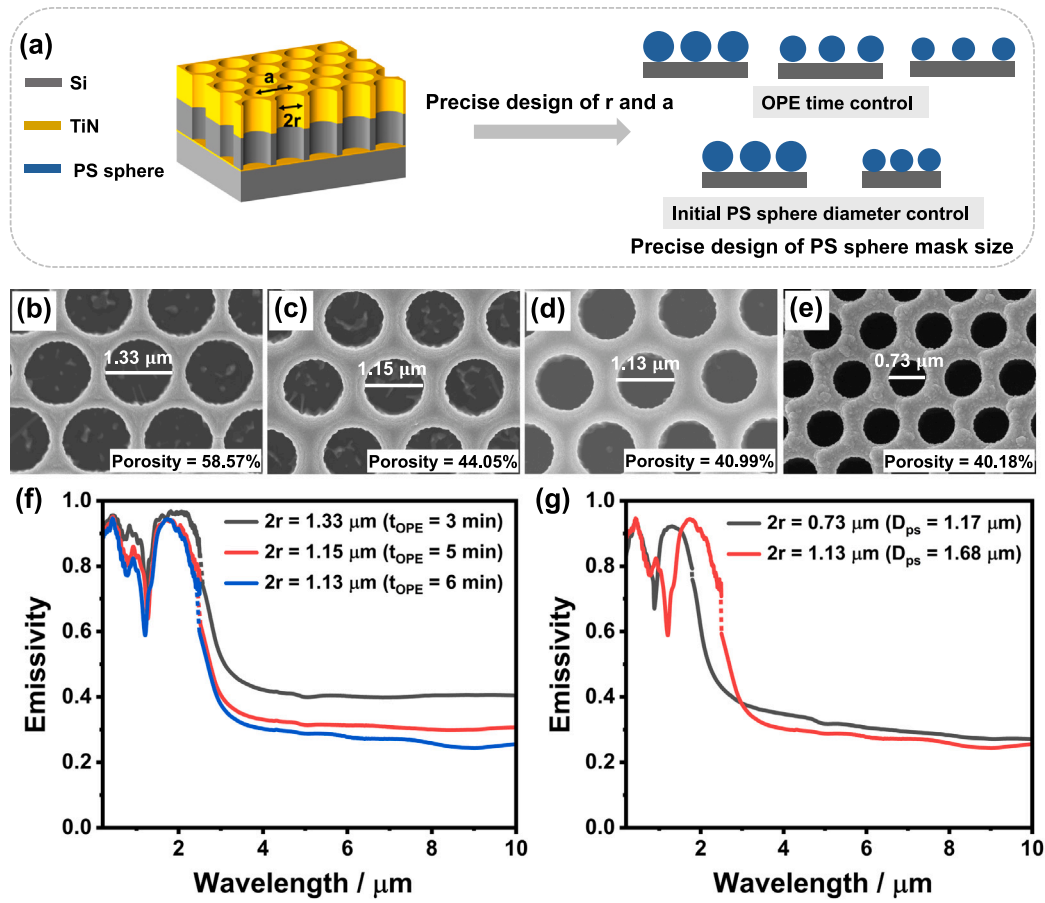


Fig. 3. (a) Schematic representation of structural parameter control of Si-TiN PhC. (b–e) SEM images of Si-TiN PhC with different radius. (f) Emission spectra of Si-TiN PhC with different OPE times. (g) Emission spectra of Si-TiN PhC with different initial PS sphere diameters.

Table 1
Comparison of some indicators of the Si-TiN PhC with different parameters.

| Sample | Porosity | Average emissivity from 200 nm to cut-off wavelength | Average emissivity from 5 μm to 10 μm |
|---|----------|--|---------------------------------------|
| 2r = 1.33 μm, a = 1.68 μm, λ _c = 2.30 μm | 58.57% | 91.61% | 40.22% |
| 2r = 1.15 μm, a = 1.68 μm, λ _c = 2.10 μm | 44.05% | 87.05% | 30.86% |
| 2r = 1.13 μm, a = 1.68 μm, λ _c = 2.00 μm | 40.99% | 84.31% | 27.02% |
| 2r = 0.73 μm, a = 1.17 μm, λ _c = 1.50 μm | 40.18% | 87.40% | 29.64% |

radiation spectrum by their room-temperature emission spectra. For the flat Si without nanostructures, the radiation spectrum decreases across the entire spectrum compared to the blackbody. In contrast, the Si-TiN PhC, with its spectral control capabilities, maintains high radiation intensity below the maximum emission wavelength of the PV cell while effectively suppressing radiation intensity beyond this wavelength to minimize waste heat. Fig. 5c shows that the output power of the PV cell increases with temperature when using both types of emitters with their I-V curves provided in Figure S6. The radiative power emitted by the emitter was calculated based on Eq. (1)

$$q_{rad} = VF \int_0^{\infty} E_b(\lambda, T) \varepsilon(\lambda) d\lambda \quad (1)$$

where VF is the geometric view factor, $\varepsilon(\lambda)$ is the emissivity of the selective emitter, and $E_b(\lambda, T)$ is the Planck blackbody radiation function [52]. The Si-TiN PhC operating at 1373 K radiated 43.72 W of power, resulting in 4.00 W of thermal power incident on the solar cell after accounting for geometric view factors. In comparison, the flat Si emitter radiated 46.29 W of power, with 4.24 W incident on the solar cell. The ratio of incident power between the two systems was comparable at $P_{PhC}/P_{flat Si} \approx 0.94$. The generated photocurrent, denoted as I_{ph} , is a key parameter in the performance of the cell. For the cell used in this work, the photocurrents generated were calculated based on Eq. (2)

$$I_{ph} = eVF \int_0^{\infty} \frac{\lambda}{hc} q_{ci}(\lambda) EQE(\lambda) d\lambda \quad (2)$$

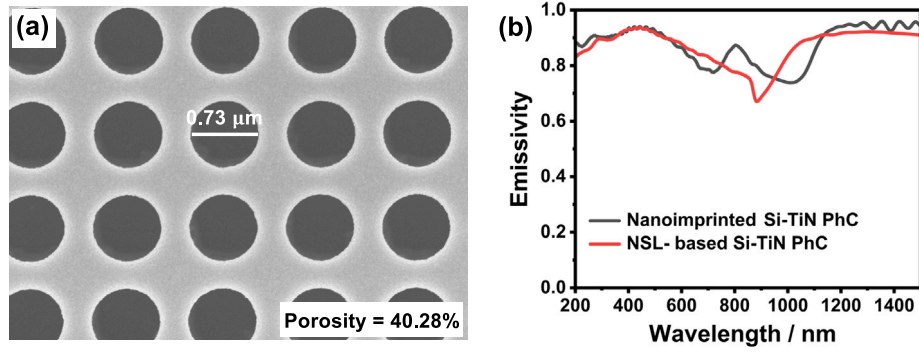


Fig. 4. (a) SEM image of nanoimprinted Si-TiN PhC. (b) Emission spectra of nanoimprinted Si-TiN PhC and NSL-based Si-TiN PhC.

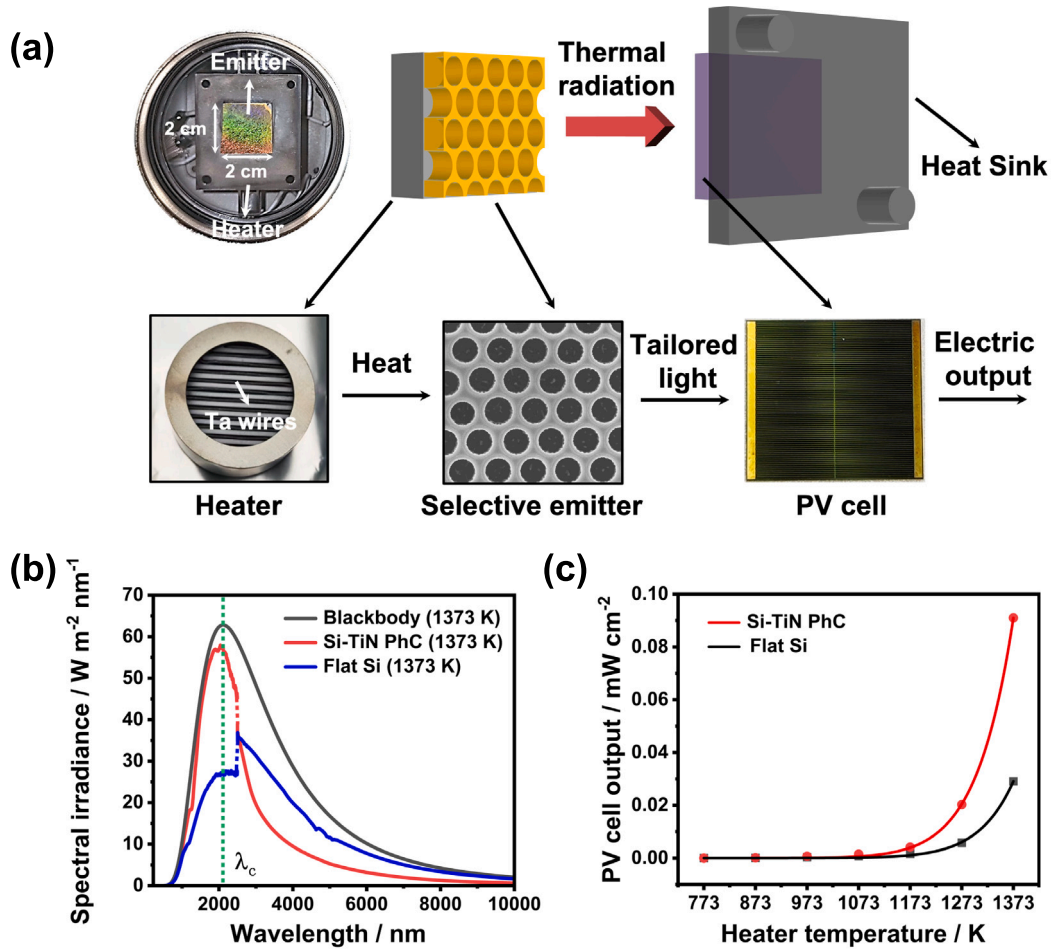


Fig. 5. (a) Illustration of the designed TPV system. The selective emitter ($2\text{ cm} \times 2\text{ cm}$) is mounted on the heat source. The triple-junction GaInP₂/InGaAs/Ge cell is $1\text{ cm} \times 1\text{ cm}$. (b) Radiation spectrum of a blackbody, Si-TiN PhC, and flat Si emitter at 1373 K. The cut-off wavelength where the Si-TiN PhC emissivity (green dashed line) is denoted as λ_c . (c) The PV cell output of the TPV system provided by the flat Si and Si-TiN PhC emitters at different temperatures.

where e is the electron charge, VF is the view factor, $\frac{hc}{\lambda}$ is the energy of a single photon, $q_{ci}(\lambda)$ is the wavelength-dependent emissive power, and $EQE(\lambda)$ is the wavelength-dependent external quantum efficiency [45]. The calculated $I_{ph}(\text{GaInP}_2, \text{PhC}) = 0.25\text{ mA}$, $I_{ph}(\text{GaInP}_2, \text{flat Si}) = 0.16\text{ mA}$; $I_{ph}(\text{InGaAs}, \text{PhC}) = 21.59\text{ mA}$, $I_{ph}(\text{InGaAs}, \text{flat Si}) = 16.20\text{ mA}$; $I_{ph}(\text{Ge}, \text{PhC}) = 914.17\text{ mA}$, $I_{ph}(\text{Ge}, \text{flat Si}) = 460.23\text{ mA}$. As observed, the photocurrents in both cases are significantly limited by the GaInP₂ junction because there are fewer high energy photons at 1373 K. However, the more than 1.53 times of generated photocurrent (0.25 mA vs. 0.16 mA) and the 3.13 times higher output power (Fig. 5c) can still demonstrate the significant benefits of spectral control

enabled by enhanced in-band emissivity. The efficiency analysis applied to different types of TPV cells reported in the literature [45] is tabulated with comparison values to blackbody emitters in Table S2 and S3. The efficiency performance of the Si-TiN PhC emitter is approximately 1.49 – 1.79 times that of blackbody emitters between 1173 K and 1473 K and comparable to that of tantalum selective emitters [53]. This demonstrates that the Si-TiN emitter achieves similar performance to tantalum while offering significantly lower fabrication costs, making it a more practical choice for large-scale applications.

The SEM image of the Si-TiN PhC after the TPV experiment is shown in Figure S7a. The TiN films and Si cavities exhibit no surface

Table 2
Comparison of the state-of-the-art absorbers/emitters with similar structures.

| Ref. | [54] | [55] | [56] | This work |
|-----------------------------------|--|---|-------------------------------------|---|
| Material | SiO ₂ /TiN/SiNx | Si/W/Al ₂ O ₃ | Si/Cr/CrN | Si/TiN |
| Structure | Grating + TiN + SiNx | Si nanopillars + W + Al ₂ O ₃ | Si nanopillars + Cr + CrN | Si cavity + TiN |
| Emission performance | 87% (250 – 2250 nm) | 95% (220 – 2600 nm) | 95% (300 – 2400 nm) | 87% (200 – 2100 nm) |
| | 29% (5 – 13 μm) | N/A | 30% (5 – 9 μm) | 31% (5 – 10 μm) |
| Thermal stability | 1073 K in vacuum | 1273 K in N ₂ atmosphere | 1373 K in N ₂ atmosphere | 1373 K in vacuum |
| Fabrication method | Continuously variable spatial frequency photolithography | Nanosphere lithography, metal-assisted chemical etching | Nanosphere lithography | Nanosphere lithography |
| Turnability of cut-off wavelength | N/A | N/A | N/A | Freely tunable by adjusting PS sphere mask size |

diffusion or cracking, demonstrating excellent high-temperature stability. Additionally, as shown in Figure S7b, the in-band and out-of-band emissivity of the Si–TiN PhC before and after the TPV experiment is nearly identical. Table 2 compares our fabrication method and results with those of other state-of-the-art absorbers or emitters with similar structures. It is evident that our emitter achieves comparable emissivity and thermal stability while utilizing only two materials and a simple structure. More importantly, by leveraging the cavity resonance principle and the controllability of the PS sphere diameter in the NSL process, emitters with arbitrary cut-off wavelengths can be precisely designed and fabricated. The flexibility, low fabrication cost, and high performance of our device enhance the feasibility of spectral control in TPV technology, bringing it closer to commercial success.

4. Conclusions

In this study, we have proposed a highly efficient and thermally stable spectrally selective emitter, based on a TiN-coated Si cavity structure, employing a straightforward and cost-effective NSL method. Because of the lossy nature of TiN, the emission bandwidth of Si cavities can be broadened. Furthermore, the versatility of the NSL method allows for precise control over the Si–TiN PhC parameters, enabling the design and fabrication of emitters with tunable cut-off wavelengths. A comparison with the emissivity of nanoimprinted PhC reveals that defects introduced by the NSL method do not impact the emission efficiency. Finally, the Si–TiN PhC was employed as a selective emitter in a TPV system, yielding an output power 3.13 times greater than that of a flat Si emitter. The morphology of the Si–TiN PhC remained intact, with no cracking or surface diffusion observed after the TPV experiments, and its in-band emission even increased after high-temperature treatment, demonstrating the potential of Si–TiN PhC as high-performance selective emitters for various high-temperature energy-conversion applications.

CRediT authorship contribution statement

Xiaoqi Zhou: Writing – original draft, Validation, Methodology, Conceptualization. **Man Zhang:** Writing – review & editing, Validation. **Shengyu Sun:** Methodology, Conceptualization. **Yixin Sun:** Resources, Conceptualization. **Zhongyan Li:** Resources, Investigation. **Shipei Zhang:** Software, Formal analysis. **Xiawa Wang:** Writing – review & editing, Supervision.

Declaration of competing interest

The authors declare that they have no known competing financial interests or personal relationships that could have appeared to influence the work reported in this paper.

Acknowledgments

This work is supported by NSFC Young Scientist Program 12105124, Gusu Innovation Program ZXL2021252, Jiangsu Shuangchuang Prestigious Ph.D Program, Kunshan Shuangchuang Talent Program kssc202202061, Kunshan Municipal Government Research Fund. We thank the Westlake Center for Micro/Nano Fabrication for its support and technical assistance. The author thanks Yuan CHENG from Instrumentation and Service Center for Molecular Sciences at Westlake University for the assistance in spectrum measurement.

Appendix A. Supplementary data

Supplementary material related to this article can be found online at <https://doi.org/10.1016/j.solmat.2025.113560>.

Data availability

Data will be made available on request.

References

- [1] H. Daneshvar, R. Prinja, N.P. Kherani, Thermophotovoltaics: Fundamentals, challenges and prospects, *Appl. Energy* 159 (2015) 560–575, <http://dx.doi.org/10.1016/j.apenergy.2015.08.064>.
- [2] D. Fan, T. Burger, S. McSherry, B. Lee, A. Lenert, S.R. Forrest, Near-perfect photon utilization in an air-bridge thermophotovoltaic cell, *Nature* 586 (2020) 237–241, <http://dx.doi.org/10.1038/s41586-020-2717-7>.
- [3] A. LaPotin, K.L. Schulte, M.A. Steiner, K. Buznitsky, C.C. Kelsall, D.J. Friedman, E.J. Tervo, R.M. France, M.R. Young, A. Rohkopf, et al., Thermophotovoltaic efficiency of 40%, *Nature* 604 (2022) 287–291, <http://dx.doi.org/10.1038/s41586-022-04473-y>.
- [4] Z. Yang, H. Li, Y. Wang, X. Chen, J. Chen, Performance comparison of near- and far-field temperature-dependent thermophotovoltaic systems with tungsten emitter and GaIn1-xAs cell, *Energy Convers. Manage.* 257 (2022) 115416, <http://dx.doi.org/10.1016/j.enconman.2022.115416>.
- [5] M. Suemitsu, T. Asano, T. Inoue, S. Noda, High-efficiency thermophotovoltaic system that employs an emitter based on a silicon rod-type photonic crystal, *ACS Photonics* 7 (2020) 80–87, <http://dx.doi.org/10.1021/acsp Photonics.9b00984>.
- [6] T. Burger, C. Sempere, B. Roy-Layinde, A. Lenert, Present efficiencies and future opportunities in thermophotovoltaics, *Joule* 4 (2020) 1660–1680, <http://dx.doi.org/10.1016/j.joule.2020.06.021>.
- [7] G. Huang, K. Wang, C.N. Markides, Efficiency limits of concentrating spectral-splitting hybrid photovoltaic-thermal (PV-T) solar collectors and systems, *Light. Sci. Appl.* 10 (2021) 28, <http://dx.doi.org/10.1038/s41377-021-00465-1>.
- [8] D.M. Bierman, A. Lenert, W.R. Chan, B. Bhatia, I. Celanović, M. Soljačić, E.N. Wang, Enhanced photovoltaic energy conversion using thermally based spectral shaping, *Nat. Energy* 1 (2016) 1–7, <http://dx.doi.org/10.1038/nenergy.2016.68>.
- [9] R. Sakakibara, V. Stelmakh, W.R. Chan, M. Ghebrehirhan, J.D. Joannopoulos, M. Soljačić, I. Čelanović, Practical emitters for thermophotovoltaics: a review, *J. Photonics Energy* 9 (2019) 032713, <http://dx.doi.org/10.1117/1.JPE.9.032713>.

- [10] Z. Wang, D. Kortge, Z. He, J. Song, J. Zhu, C. Lee, H. Wang, P. Bermel, Selective emitter materials and designs for high-temperature thermophotovoltaic applications, *Sol. Energy Mater. Sol. Cells* 238 (2022) 111554, <http://dx.doi.org/10.1016/j.solmat.2021.111554>.
- [11] U.C. Pernisz, C.K. Saha, Silicon carbide emitter and burner elements for a TPV converter, *AIP Conf. Proc.* 321 (1) (1995) 99–105, <http://dx.doi.org/10.1063/1.47060>.
- [12] G. Torsello, M. Lomascolo, A. Licciulli, D. Diso, S. Tundo, M. Mazzer, The origin of highly efficient selective emission in rare-earth oxides for thermophotovoltaic applications, *Nat. Mater.* 3 (2004) 632–637, <http://dx.doi.org/10.1038/nmat1197>.
- [13] M. Zeyghami, E. Stefanakos, D.Y. Goswami, Development of one-dimensional photonic selective emitters for energy harvesting applications, *Sol. Energy Mater. Sol. Cells* 163 (2017) 191–199, <http://dx.doi.org/10.1016/j.solmat.2017.01.026>.
- [14] W. Zhang, B. Wang, C. Zhao, Selective thermophotovoltaic emitter with aperiodic multilayer structures designed by machine learning, *ACS Appl. Energy Mater.* 4 (2) (2021) 2004–2013, <http://dx.doi.org/10.1021/acsaem.0c03201>.
- [15] L. Li, X. Wu, H. Liu, Z. Yang, Y. Liu, K. Yu, High-performance near-field thermophotovoltaics based on multilayer hyperbolic materials, *Int. J. Heat Mass Transfer* 230 (2024) 125783, <http://dx.doi.org/10.1016/j.ijheatmasstransfer.2024.125783>.
- [16] Y.X. Yeng, J.B. Chou, V. Rinnerbauer, Y. Shen, S.-G. Kim, J.D. Joannopoulos, M. Soljačić, I. Čelanović, Global optimization of omnidirectional wavelength selective emitters/absorbers based on dielectric-filled anti-reflection coated two-dimensional metallic photonic crystals, *Opt. Express* 22 (2014) 21711–21718, <http://dx.doi.org/10.1364/OE.22.021711>.
- [17] R. Sakakibara, V. Stelmakh, W.R. Chan, R.D. Geil, S. Krämer, T. Savas, M. Ghebrehrihan, J.D. Joannopoulos, M. Soljačić, I. Čelanović, A high-performance, metallo-dielectric 2D photonic crystal for thermophotovoltaics, *Sol. Energy Mater. Sol. Cells* 238 (2022) 111536, <http://dx.doi.org/10.1016/j.solmat.2021.111536>.
- [18] M. Garín, D. Hernández, T. Trifonov, R. Alcubilla, Three-dimensional metallo-dielectric selective thermal emitters with high-temperature stability for thermophotovoltaic applications, *Sol. Energy Mater. Sol. Cells* 134 (2015) 22–28, <http://dx.doi.org/10.1016/j.solmat.2014.11.017>.
- [19] A. Chirumamilla, Y. Yang, M.H. Salazar, F. Ding, D. Wang, P.K. Kristensen, P. Fojan, S.I. Bozhevolnyi, D.S. Sutherland, K. Pedersen, M. Chirumamilla, Spectrally selective emitters based on 3D Mo nanopillars for thermophotovoltaic energy harvesting, *Mater. Today Phys.* 21 (2021) 100503, <http://dx.doi.org/10.1016/j.mtphys.2021.100503>.
- [20] C. Meng, Y. Liu, Z. Xu, H. Wang, X. Tang, Selective emitter with core-shell nanosphere structure for thermophotovoltaic systems, *Energy* 239 (2022) 121884, <http://dx.doi.org/10.1016/j.energy.2021.121884>.
- [21] K. Yuan, B. Chen, S. Shan, J. Xu, Q. Yang, Tunable narrowband metamaterial thermophotovoltaic emitter: Ideal performance analysis and structural design based on photovoltaic cell performance matching, *Energy Convers. Manage.* 312 (2024) 118556, <http://dx.doi.org/10.1016/j.enconman.2024.118556>.
- [22] J. Wang, Z. Wu, Y. Liu, S. Hou, Y. Qiao, Z. Tang, J. Mao, Q. Zhang, F. Cao, High-selectivity planar thermal emitter with a stable temperature over 1400 K for a thermophotovoltaic system, *ACS Appl. Mater. Interfaces* 15 (42) (2023) 49123–49131, <http://dx.doi.org/10.1021/acsmi.3c10191>.
- [23] A. Chirumamilla, Y. Yang, M.H. Salazar, F. Ding, D. Wang, P.K. Kristensen, P. Fojan, S.I. Bozhevolnyi, D.S. Sutherland, K. Pedersen, et al., Spectrally selective emitters based on 3D Mo nanopillars for thermophotovoltaic energy harvesting, *Mater. Today Phys.* 21 (2021) 100503, <http://dx.doi.org/10.1016/j.mtphys.2021.100503>.
- [24] H. Zhang, C. Wang, Y. Shu, J. Liu, K. Ren, F.-Q. Dou, Tunability of a broad-band selective metamaterial emitter in thermophotovoltaic systems, *Int. J. Heat Mass Transfer* 216 (2023) 124583, <http://dx.doi.org/10.1016/j.ijheatmasstransfer.2023.124583>.
- [25] K. Yuan, B. Chen, S. Shan, J. Xu, Q. Yang, Tunable narrowband metamaterial thermophotovoltaic emitter: Ideal performance analysis and structural design based on photovoltaic cell performance matching, *Energy Convers. Manage.* 312 (2024) 118556, <http://dx.doi.org/10.1016/j.enconman.2024.118556>.
- [26] T. Huang, B. Wang, C. Zhao, A novel selective thermophotovoltaic emitter based on multipole resonances, *Int. J. Heat Mass Transfer* 182 (2022) 122039, <http://dx.doi.org/10.1016/j.ijheatmasstransfer.2021.122039>.
- [27] H. Sai, H. Yugami, Thermophotovoltaic generation with selective radiators based on tungsten surface gratings, *Appl. Phys. Lett.* 85 (2004) 3399–3401, <http://dx.doi.org/10.1063/1.1807031>.
- [28] I. Čelanović, N. Jovanović, J. Kassakian, Two-dimensional tungsten photonic crystals as selective thermal emitters, *Appl. Phys. Lett.* 92 (2008) 193101, <http://dx.doi.org/10.1063/1.2927484>.
- [29] Y.X. Yeng, M. Ghebrehrihan, P. Bermel, W.R. Chan, J.D. Joannopoulos, M. Soljačić, I. Čelanović, Enabling high-temperature nanophotonics for energy applications, *Proc. Natl. Acad. Sci. USA* 109 (2012) 2280–2285, <http://dx.doi.org/10.1073/pnas.1120149109>.
- [30] V. Rinnerbauer, A. Lenert, D.M. Bierman, Y.X. Yeng, W.R. Chan, R.D. Geil, J.J. Senkevich, J.D. Joannopoulos, E.N. Wang, M. Soljačić, I. Čelanović, Metallic photonic crystal absorber-emitter for efficient spectral control in high-temperature solar thermophotovoltaics, *Adv. Energy Mater.* 4 (2014) 1400334, <http://dx.doi.org/10.1002/aenm.201400334>.
- [31] M. Araghchini, Y.X. Yeng, N. Jovanović, P. Bermel, L.A. Kolodziejski, M. Soljačić, I. Čelanović, J.D. Joannopoulos, Fabrication of two-dimensional tungsten photonic crystals for high-temperature applications, *J. Vac. Sci. Technol. B* 29 (2011) 061402, <http://dx.doi.org/10.1116/1.3646475>.
- [32] J.-M. Kim, K.-H. Park, D.-S. Kim, B. yeon Hwang, S.-K. Kim, H.-M. Chae, B.-K. Ju, Y.-S. Kim, Design and fabrication of spectrally selective emitter for thermophotovoltaic system by using nano-imprint lithography, *Appl. Surf. Sci.* 429 (2018) 138–143, <http://dx.doi.org/10.1016/j.apsusc.2017.07.300>.
- [33] F. Xiu, H. Lin, M. Fang, G. Dong, S. Yip, J.C. Ho, Fabrication and enhanced light-trapping properties of three-dimensional silicon nanostructures for photovoltaic applications, *Pure Appl. Chem.* 86 (5) (2014) 557–573, <http://dx.doi.org/10.1515/pac-2013-1119>.
- [34] S. Chen, T. Zhu, F. Juan, Y. Zhu, J. Xu, K. Chen, High-temperature stable and efficient broadband solar absorber based on Si/metal plasmonic structures, *Sol. Energy* 276 (2024) 112664, <http://dx.doi.org/10.1016/j.solener.2024.112664>.
- [35] N. Kwon, K. Kim, S. Sung, I. Yi, I. Chung, Highly conductive and transparent ag honeycomb mesh fabricated using a monolayer of polystyrene spheres, *Nanotechnology* 24 (2013) 235205, <http://dx.doi.org/10.1088/0957-4484/24/23/235205>.
- [36] V. Rinnerbauer, S. Ndao, Y. Xiang Yeng, J.J. Senkevich, K.F. Jensen, J.D. Joannopoulos, M. Soljačić, I. Čelanović, R.D. Geil, Large-area fabrication of high aspect ratio tantalum photonic crystals for high-temperature selective emitters, *J. Vac. Sci. Technol. B* 31 (2012) 011802, <http://dx.doi.org/10.1116/1.4771901>.
- [37] B. Chang, P. Leussink, F. Jensen, J. Hübner, H. Jansen, DREM: Infinite etch selectivity and optimized scallop size distribution with conventional photoresists in an adapted multiplexed bosch DRIE process, *Microelectron. Eng.* 191 (2018) 77–83, <http://dx.doi.org/10.1016/j.mee.2018.01.034>.
- [38] B. Chang, F. Jensen, J. Hübner, H. Jansen, DREM2: a facile fabrication strategy for freestanding three dimensional silicon micro- and nanostructures by a modified bosch etch process, *J. Micromech. Microeng.* 28 (2018) 105012, <http://dx.doi.org/10.1088/1361-6439/aa00c4>.
- [39] K.-W. Jo, S.-S. Yun, N. Punithavelan, S. Ho Jeong, S. kyu Lee, J.-H. Lee, Conformability and optical reflectance of Ti/Au film sputtered on the Si vertical sidewalls, *J. Vac. Sci. Technol. B* 23 (2005) 2095–2101, <http://dx.doi.org/10.1116/1.2052712>.
- [40] W.-P. Guo, R. Mishra, C.-W. Cheng, B.-H. Wu, L.-J. Chen, M.-T. Lin, S. Gwo, Titanium nitride epitaxial films as a plasmonic material platform: Alternative to gold, *ACS Photonics* 6 (2019) 1848–1854, <http://dx.doi.org/10.1021/acsp Photonics.9b00617>.
- [41] Y. Zhu, G. Hou, Q. Wang, T. Zhu, T. Sun, J. Xu, K. Chen, Silicon-based spectrally selective emitters with good high-temperature stability on stepped metasurfaces, *Nanoscale* 14 (2022) 10816–10822, <http://dx.doi.org/10.1039/D2NR02299K>.
- [42] D. Jiang, W. Yang, Refractory material based frequency selective emitters/absorbers for high efficiency and thermal stable thermophotovoltaics, *Sol. Energy Mater. Sol. Cells* 163 (2017) 98–104, <http://dx.doi.org/10.1016/j.solmat.2017.01.022>.
- [43] T. Krekeler, S.S. Rout, G.V. Krishnamurthy, M. Störmer, M. Arya, A. Ganguly, D.S. Sutherland, S.I. Bozhevolnyi, M. Ritter, K. Pedersen, A.Y. Petrov, M. Eich, M. Chirumamilla, Unprecedented thermal stability of plasmonic titanium nitride films up to 1400 ° C, *Adv. Opt. Mater.* 9 (2021) 2100323, <http://dx.doi.org/10.1002/adom.202100323>.
- [44] Y. Chen, H. Li, J. Chen, D. Li, M. Zhang, G. Yu, L. Jiang, Y. Zong, B. Dong, Z. Zeng, et al., Self-generating nanogaps for highly effective surface-enhanced Raman spectroscopy, *Nano Res.* 15 (2022) 3496–3503, <http://dx.doi.org/10.1007/s12274-021-3924-8>.
- [45] W. Chan, R. Huang, C. Wang, J. Kassakian, J. Joannopoulos, I. Čelanović, Modeling low-bandgap thermophotovoltaic diodes for high-efficiency portable power generators, *Sol. Energy Mater. Sol. Cells* 94 (3) (2010) 509–514, <http://dx.doi.org/10.1016/j.solmat.2009.11.015>.
- [46] M.G. Mauk, Survey of thermophotovoltaic (TPV) devices, in: A. Krier (Ed.), *Mid-infrared Semiconductor Optoelectronics*, Springer London, London, 2006, pp. 673–738, http://dx.doi.org/10.1007/1-84628-209-8_21.
- [47] W.R. Chan, V. Stelmakh, M. Ghebrehrihan, M. Soljačić, J.D. Joannopoulos, I. Čelanović, Enabling efficient heat-to-electricity generation at the mesoscale, *Energy Env. Sci.* 10 (2017) 1367–1371, <http://dx.doi.org/10.1039/C7EE00366H>.
- [48] Y. Tian, X. Liu, A. Ghanekar, Y. Zheng, Scalable-manufactured metal-insulator-metal based selective solar absorbers with excellent high-temperature insensitivity, *Appl. Energy* 281 (2021) 116055, <http://dx.doi.org/10.1016/j.apenergy.2020.116055>.
- [49] Y. Wang, M. Zhang, Y. Lai, L. Chi, Advanced colloidal lithography: From patterning to applications, *Nano Today* 22 (2018) 36–61, <http://dx.doi.org/10.1016/j.nantod.2018.08.010>.
- [50] Y. Liu, L. Tang, J. Shao, Y. Tang, J. Li, X. Lv, Y. Yuan, Experimental performance comparison of 0.72 eV-GaSb and 0.59 eV-InGaAs thermophotovoltaic cells under different radiation temperatures, *Appl. Energy* 361 (2024) 122959, <http://dx.doi.org/10.1016/j.apenergy.2024.122959>.
- [51] A. Lenert, D.M. Bierman, Y. Nam, W.R. Chan, I. Čelanović, M. Soljačić, E.N. Wang, A nanophotonic solar thermophotovoltaic device, *Nat. Nanotechnol.* 9 (2014) 126–130, <http://dx.doi.org/10.1038/nnano.2013.286>.

- [52] E.J. Tervo, R.M. France, D.J. Friedman, M.K. Arulanandam, R.R. King, T.C. Narayan, C. Luciano, D.P. Nizamian, B.A. Johnson, A.R. Young, L.Y. Kuritzky, E.E. Perl, M. Limpinsel, B.M. Kayes, A.J. Ponc, D.M. Bierman, J.A. Briggs, M.A. Steiner, Efficient and scalable GaInAs thermophotovoltaic devices, *Joule* 6 (11) (2022) 2566–2584, <http://dx.doi.org/10.1016/j.joule.2022.10.002>.
- [53] X. Wang, R. Liang, P. Fisher, W. Chan, J. Xu, Radioisotope thermophotovoltaic generator design methods and performance estimates for space missions, *J. Propuls. Power* 36 (4) (2020) 593–603, <http://dx.doi.org/10.2514/1.B37623>.
- [54] S. Wu, Y. Ye, Z. Jiang, T. Yang, L. Chen, Large-area, ultrathin metasurface exhibiting strong unpolarized ultrabroadband absorption, *Adv. Opt. Mater.* 7 (2019) 1901162, <http://dx.doi.org/10.1002/adom.201901162>.
- [55] G. Hou, Z. Wang, J. Xu, K. Chen, Tungsten-coated silicon nanopillars as ultra-broadband and thermally robust solar harvesting materials, *ACS Appl. Nano Mater.* 3 (2020) 2430–2437, <http://dx.doi.org/10.1021/acsnm.9b02542>.
- [56] S. Chen, T. Zhu, F. Juan, Y. Zhu, J. Xu, K. Chen, High-temperature stable and efficient broadband solar absorber based on si/metal plasmonic structures, *Sol. Energy* 276 (2024) 112664, <http://dx.doi.org/10.1016/j.solener.2024.112664>.